

Full length article

Ductile CoCrFeNiMo_x high entropy alloys strengthened by hard intermetallic phases

W.H. Liu ^a, Z.P. Lu ^b, J.Y. He ^b, J.H. Luan ^a, Z.J. Wang ^c, B. Liu ^d, Yong Liu ^d, M.W. Chen ^e, C.T. Liu ^{a,*}

^a Center for Advanced Structural Materials, Department of Mechanical and Biomedical Engineering, City University of Hong Kong, Hong Kong, China

^b State Key Laboratory for Advance Metals and Materials, University of Science and Technology Beijing, Beijing 10083, PR China

^c State Key Laboratory of Solidification Processing, Northwestern Polytechnical University, Xi'an 710072, PR China

^d State Key Laboratory for Powder Metallurgy, Central South University, Changsha 410083, PR China

^e WPI Advanced Institute for Materials Research, Tohoku University, Sendai 980-8577, Japan

ARTICLE INFO

Article history:

Received 18 April 2016

Received in revised form

27 June 2016

Accepted 28 June 2016

Available online 5 July 2016

Keywords:

High entropy alloys

Precipitation hardening

Crack propagation

Intermetallic phase

Strain hardening

ABSTRACT

Face-centered-cubic (fcc) type high entropy alloys (HEAs) exhibit outstanding ductility even at the liquid nitrogen temperature, but they are relatively weak in strength which is far from the requirements for practical structural applications. One of the general concepts employed previously in alloy design is the suppression of ‘brittle’ intermetallic compound formation which usually leads to a serious embrittlement. Surprisingly, we reveal in this study that the precipitation of hard σ and μ intermetallic compounds tremendously strengthened the CoCrFeNiMo_{0.3} HEA but without causing a serious embrittlement. It exhibits a tensile strength as high as 1.2 GPa and a good ductility of ~19%. A careful study of the deformation behavior reveals that the fcc matrix exhibits an extremely high work hardening exponent of 0.75, which suppresses the propagation of microcracks originated at these brittle particles. Our work presents a very successful demonstration of using complex hard intermetallic particles to manipulate the properties of fcc-type HEA systems. Furthermore, lattice distortion has been carefully measured in powder-metallurgy materials by line broadening from X-ray diffraction (XRD). It is interesting to discover that lattice planes are highly distorted in HEAs and this distortion also contributes to solid solution hardening.

© 2016 Acta Materialia Inc. Published by Elsevier Ltd. All rights reserved.

1. Introduction

A new concept of alloy system, referred as HEAs, has been proposed recently, which abandons the “base-element” idea and adopts a mixture of multiple principle elements in an equimolar or near-equimolar ratio to form multi-component alloys [1,2]. Conceptually, this is a radical departure from the conventional notions and opens up a huge alloy design space yet to be fully explored by us [2–5]. Due to their high mixing entropy, these alloys tend to form a simple solution-like phase [2,4–7] and show a variety of interesting and unusual properties [8–13]. Among them fcc-type HEAs, such as CoCrFeNiMn [14–16], exhibit outstanding ductility and fracture toughness even down to the liquid nitrogen temperature [11]. However, they are relatively weak in strength for

structural applications [17]. The important scientific and technical approach for structural use of these HEAs is how to effectively harden them but without causing a serious embrittlement.

Homogeneous precipitation of hard intermetallic particles has been recognized as a powerful method for strengthening steels and alloys because of their resistance to gliding dislocations [18,19]. Unfortunately, strength and ductility are mutually exclusive. One of the general concepts employed commonly in the alloy design of high performance materials has been the suppression of ‘brittle’ intermetallic compound formation. It is well known that the precipitation of hard topologically close-packed (TCP) phases, such as σ and μ phases which usually have an extremely high hardness in the order of 15 GPa [20], has caused a noticeable degradation of overall high-temperature performance of Ni-based superalloys, the state-of-the-art high temperature materials, because the Ni-based matrix has limited ductility which can't suppress the brittle cracking of TCP phases [21], thus their formation has to be absolutely avoided via composition control. However, the outstanding

* Corresponding author.

E-mail address: chainliu@cityu.edu.hk (C.T. Liu).

ductility of the CoCrFeNi HEA (elongation of ~59%) is possibly to serve as a good base for hard particle precipitation strengthening and the precipitation of L₁₂-Ni₃ (Ti,Al) intermetallic phase in this matrix has proved the effectiveness of intermetallic phases in strengthening [22]. In this study, we, against the common alloy design principle, are on purposely added these hard but brittle TCP intermetallic phases in the CoCrFeNi HEA, which would require a careful modification of the chemical composition of the alloy.

In this study, the alloying additions of Mo were added into the CoCrFeNi matrix. Mo has a moderately large atomic size for both solid solution and precipitation hardening. Furthermore, it is known that Mo is capable of forming hard intermetallic phases with Co, Cr, Fe, and Ni elements. Also, despite their poor plasticity in the bulk state at ambient temperatures, Mo-based intermetallics usually offer an attractive combination of physical and mechanical properties such as good thermal stability, oxidation and wear resistance. Thus, Mo is selected as a promising element added to the CoCrFeNi HEA for precipitation hardening. Furthermore, in this work a computational-aided alloy design approach was employed to guide the alloy design and the calculated pseudo binary diagram of the (CoCrFeNi)-Mo system is presented in Fig. 1 by the CALPHAD method [23]. According to this diagram, Mo has limited solubility in the fcc matrix. For example, the CoCrFeNiMo_{0.3} alloy (see Table 1) containing 6.96 at.% Mo is in a single fcc phase at 1500 K, but on quenching and aging below the temperature, there is the possibility of forming σ and μ intermetallic compounds. Consequently, the microstructure of the alloy can be varied by careful control of thermal treatment.

The purpose of this work is three folds. First is to obtain a fundamental understanding of the local lattice distortion in HEAs. Nonetheless, XRD intensity obtained from cast samples usually has a large preferred crystallographic orientation effect (i.e. texture) [24], the data of which can't be used to analyze and measure the local lattice distortion. In our study, powder metallurgy was thus employed to reduce the preferred orientation effects in order to quantitatively reveal the local lattice distortion in HEAs. The second purpose is to develop ultra-high strength HEAs by introducing an optimum amount of hard intermetallic phases. Third is to

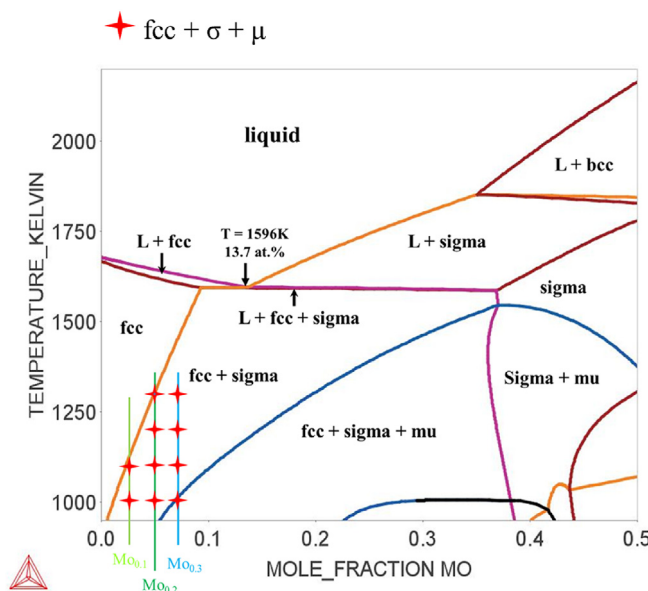


Fig. 1. The pseudo binary phase diagram of the (CoCrFeNi)-Mo alloy system. Star stands a mixture of the fcc, σ and μ phases in the Mo_x ($x = 0.1, 0.2$ and 0.3) at 973 K, 1173 K, 1273 K.

Table 1

Chemical composition of the as-cast Mo_x ($x = 0, 0.1, 0.2$ and 0.3) alloys and the Mo_{0.3} alloy 60%-rolled and annealed at different conditions.

As cast alloys	Phase	Fe at.%	Co at.%	Ni at.%	Cr at.%	Mo at.%
Mo ₀ alloy	Nominal	25	25	25	25	—
	Matrix	28.21	24.33	25.87	21.90	—
Mo _{0.1} alloy	Nominal	24.39	24.39	24.39	24.39	2.44
	Matrix	28.08	24.87	24.91	19.64	2.50
Mo _{0.2} alloy	Nominal	23.81	23.81	23.81	23.81	4.76
	Interdendritic	24.84	20.80	22.98	21.45	9.93
	Dendritic	26.89	24.98	24.92	18.37	4.85
Mo _{0.3} alloy	Nominal	23.26	23.26	23.26	23.26	6.96
	Matrix	26.44	23.65	25.06	18.27	6.58
	σ phase	20.01	19.81	14.77	21.81	23.59
1073 K/3 ds	Matrix	23.26	24.01	24.04	20.64	7.95
	σ phase	15.91	17.29	10.78	27.54	28.48
	μ phase	15.13	18.89	12.90	18.70	34.38
1123 K/1 h	Matrix	22.96	24.20	23.60	23.01	6.23
	σ phase	19.60	18.75	14.95	29.76	16.94
	μ phase	20.63	22.84	22.11	21.97	12.45
1173 K/5 h	Matrix	24.91	23.31	23.10	22.73	5.97
	σ phase	17.14	18.89	11.03	33.55	19.39
	μ phase	18.36	19.89	13.94	23.27	25.54

mechanistically understand the crack nucleation and propagation in a very ductile fcc matrix.

2. Experimental

The chemical compositions of the CoCrFeNiMo_x ($x = 0, 0.1, 0.11, 0.18, 0.2, 0.23$ and 0.3 , corresponding to 0, 2.44, 2.68, 4.31, 4.76, 5.44 and 6.96 at.%) alloy system used in this study are listed in Tables 1 and 2. For convenience, they are referred to as Mo₀, Mo_{0.1}, Mo_{0.11}, Mo_{0.18}, Mo_{0.2}, Mo_{0.23} and Mo_{0.3}. The as-cast Mo_x ($x = 0, 0.1, 0.2$ and 0.3) alloys were fabricated through melting and casting in a vacuum system back-filled with pure Ar cover gas in a laboratory-scale arc furnace, resulting in an ingot size of $50 \times 15 \times 3$ mm. The ingot was annealed at 500°C for 4 h and then air cooled to release the residual stress caused by rapid cooling during casting. Moreover, the CoCrFeNiMo_x ($x = 0, 0.11, 0.18$ and 0.23) HEAs were also prepared by powder metallurgy method. High purity metals of Fe, Co, Cr, Ni and Mo were put in a water-cooled copper crucible and melted in an induction heated vacuum furnace. The melt was then drop through a ceramic tube, and atomized by high purity Ar. The atomization pressure, metal flow rate and gas flow rate were 4 MPa, 50 g/s and $0.25 \text{ m}^3 \text{ s}^{-1}$, respectively. The liquid droplets flied in the atomization chamber, cooled down and solidified to spherical powders. The alloy powders were gathered in a gas tight powder can. The subsequent powder handling and the filling of the extrusion cans were all performed in a purified Ar atmosphere. The composition of the gas-atomized powders was analyzed by inductive coupling plasma (ICP) emission spectrograph, and the oxygen content was determined by the fusion method on a Leco O/N analyzer and the result was list in Table 2. To evaluate the stable phase constitution at

Table 2

The ICP element analyses of the Mo_x ($x = 0, 0.11, 0.18$ and 0.23) alloy powders (at.%).

Powders	Composition	Fe at.%	Co at.%	Cr at.%	Ni at.%	Mo at.%
Mo ₀	Nominal	25	25	25	25	—
	ICP analysis	23.49	25.51	25.31	25.31	—
Mo _{0.11}	Nominal	24.33	24.33	24.33	24.33	2.68
	ICP analysis	24.03	24.87	24.43	23.89	2.78
Mo _{0.18}	Nominal	23.92	23.92	23.92	23.92	4.31
	ICP analysis	25.70	22.74	23.99	23.23	4.34
Mo _{0.23}	Nominal	23.64	23.64	23.64	23.64	5.44
	ICP analysis	25.05	22.33	23.96	23.12	5.54

medium temperature range, the as cast $\text{Mo}_{0.1}$, $\text{Mo}_{0.2}$ and $\text{Mo}_{0.3}$ alloys with 3 mm thickness was cold-rolled to 1.2 mm (a reduction of 60%) intermittently, and then annealed at 973 K for 3 ds, 1073 K for 3 ds, 1173 K for 2 ds and 1273 K for 1 d, respectively, and immediately water-quenched. To obtain a holistic understanding of the hardening effects of the precipitated σ and μ particles on the tensile properties of the $\text{Mo}_{0.3}$ alloy, the $\text{Mo}_{0.3}$ alloy was 60%-rolled and annealed at 1123 K for 1 h and 1173 K for 5 h, separately.

XRD analysis was performed using $\text{CuK}\alpha$ radiation (MXP21VAHF). The microstructures were characterized using a Zeiss Supra55 scanning electron microscope (SEM) and a JEM-2010 high-resolution transmission electron microscope (TEM) coupled with energy dispersive spectrometer (EDS). SEM specimens were initially polished to 2000-grit SiC paper and, subsequently, electrochemically polished for the final surface clarification using a $\text{HClO}_4:\text{C}_2\text{H}_6\text{O} = 1:9$ solution with a direct voltage of 30 V at room temperature. TEM samples were primarily punched to $\Phi 3$ mm circle sheets and then ground to about 50 μm , followed by twin-jet electro-polishing using a mixed solution of $\text{HNO}_3:\text{CH}_4\text{O} = 1:4$ under a temperature around 233 K.

The nanoindentation hardness tests were performed on the TI 950 TribolIndenter system (Hysitron Inc., Minneapolis, MN) with a Berkovich indenter at room temperature, with loading rate 1.5 mN s^{-1} and peak load 6.0 mN. Tensile tests were carried out on a CMT4105 universal electronic tensile testing machine with a strain rate of $1 \times 10^{-3} \text{ s}^{-1}$ at room temperature. Sheet tensile samples with a cross-section of 4×1.2 mm and a gauge length of 12.5 mm were prepared by electro discharge machining. Surface of test samples was polished down to a 2000-grit SiC paper to eliminate scratches.

3. Results

3.1. XRD on the cast alloys and powder forms

HEAs in both cast and powder-metallurgy forms were prepared. The XRD results obtained from the stress-relieved cast Mo_x ($x = 0, 0.1, 0.2$ and 0.3) alloys are shown in Fig. 2a. There appears to be only the fcc phase in the cast state of the Mo_0 , $\text{Mo}_{0.1}$ and $\text{Mo}_{0.2}$ alloys but obvious [200] texture can be seen from the abnormal peak intensity ratios. However, an indication of σ phase with a tetragonal structure appears to form in the $\text{Mo}_{0.3}$ alloy. Powder metallurgy with a fast cooling rate was employed to reduce the preferred orientation effects observed in the cast alloys, the result of which could be used for accurately measuring the local lattice distortion. The powder diffractions are presented in Fig. 2b, and only the fcc diffraction peaks are observed for all the Mo_x ($x = 0, 0.11, 0.18$ and 0.23) powders (see Table 2). Fig. 2c shows a result of Rietveld analysis on the XRD pattern of the Mo_0 powder whose crystal structure was shown here [25]. Clearly, the XRD results are in a good accordance with the theoretical values, indicating that the preferred orientation effects were eliminated in the powder materials. Fig. 2d presents the peak intensity variation of $(111)_{\text{fcc}}$ of the powders indicating clearly that the peak intensity decreases steadily with the Mo concentration. This confirms the previous report [24] that the intrinsic lattice distortion could cause the anomalous decrease in the XRD intensities. Furthermore, the XRD results of the $\text{Mo}_{0.3}$ alloy 60%-rolled and followed by annealing at 973 K for 3 ds, 1073 K for 3 ds, 1173 K for 2 ds, 1273 K for 1 d, 1123 K for 1 h and 1173 K for 5 h are also included in Fig. 2e. It can be seen that besides the σ phase and the fcc matrix there another μ phase with a rhombohedral structure precipitated in the $\text{Mo}_{0.3}$ alloy at the temperature range of 973–1273 K.

3.2. CALPHAD analysis and phase stability

The thermo-Calc computer program together with a validated database for the thermodynamic calculations of phase equilibrium based on the CALPHAD method [23] has been currently used for the evaluation of phase stability in the complex multi-component systems. However, its application in HEAs with equiatomic or close-to-equiatomic compositions has been sporadic so far due to the loss of solvent. In this study, the pseudo-binary phase diagram of (CoCrFeNi)-Mo was calculated using the software Thermo-Calc 3.0.1. In view of the fact that both Fe and Co can form continuous solid solutions with Ni at almost the full composition range, we simply took the (CoCrFeNi)-Mo alloys as the Ni-based alloys, and the preliminary calculations were then based on the TTNI8 database for Ni-based alloys. The results so obtained are presented in Fig. 1.

To evaluate the accuracy of the pseudo binary diagram in Fig. 1, the microstructures of the as-cast Mo_x ($x = 0, 0.1, 0.2$ and 0.3) alloys and the $\text{Mo}_{0.3}$ alloy 60% cold rolled and annealed at different conditions are examined and presented in Fig. 3. The as-cast Mo_0 and $\text{Mo}_{0.1}$ alloys exhibit a single phase polycrystalline structure (Fig. 3a and b). With the increased Mo additions, the microstructures of the as-cast $\text{Mo}_{0.2}$ and $\text{Mo}_{0.3}$ alloys (Fig. 3c–d) evolve to a dendritic structure, and Mo starts to segregate in the interdendritic areas in the as-cast $\text{Mo}_{0.3}$ alloy (Fig. 3d) showing a mixed two-phase structure (see the inset of Fig. 3d). The TEM image and the selected-area diffraction (SEAD) pattern in Fig. 3m showing a large precipitate embodied in the fcc matrix of the as-cast $\text{Mo}_{0.3}$ alloy clearly confirm that the precipitate consists of a mixture of the fcc and the σ phases, which are enriched with Cr and Mo elements (Table 1). Noted that the fcc phase particles were precipitated out from the σ particle during cooling from a high temperature on casting. Thus, this complex structure can be simply referred as a “double precipitation” during cooling down on casting, which can be explained by the pseudo binary diagram in Fig. 1.

The phases formed in the cast HEAs are essentially metastable: they are indeed the firstly formed solid-state phases upon solidification, which are then kept to the ambient temperature due to the sluggish diffusion kinetics of HEAs. To investigate the stable phase constitution at different conditions, the $\text{Mo}_{0.1}$, $\text{Mo}_{0.2}$ and $\text{Mo}_{0.3}$ alloys were 60%-rolled and annealed at 973 K for 3 ds, 1073 K for 3 ds, 1173 K for 2 ds and 1273 K for 1 d, respectively, and the representative microstructures of the $\text{Mo}_{0.3}$ alloy at the four annealed states are presented in Fig. 3e–h. Clearly a number of particles precipitated out during the treatments. The TEM image and SEAD pattern of the 60%-rolled $\text{Mo}_{0.3}$ annealed for 3 ds at 1073 K are shown in Fig. 3n. It was identified that a (Mo,Cr)-rich μ phase precipitated in the fcc matrix which is in consistent with the XRD result in Fig. 2e beside the (Cr,Mo)-rich σ phase during the annealing process. Such composition difference makes the μ phase much brighter in contrast than the σ phase in the backscattered SEM images as marked in Fig. 3e–l. The microstructures of the $\text{Mo}_{0.2}$ and $\text{Mo}_{0.3}$ alloys consist of the precipitation of the σ and μ phases in the fcc matrix at the temperature range of 973–1273 K (as marked by stars in Fig. 1), while this region shrinks to 973–1073 K in the $\text{Mo}_{0.1}$ alloy. It can be concluded that the pseudo phase diagram quite successfully predicts all the structural features in the current alloy system. However, the solubility of Mo in the fcc matrix at medium temperatures should be lower than that in the pseudo phase diagram and the “fcc + sigma + mu” zone should be more broadened while the “fcc + sigma” zone should be more narrowed in Fig. 1.

3.3. Precipitation phases and morphologies

Here we tried to utilize the brittle but hard σ and μ particles as

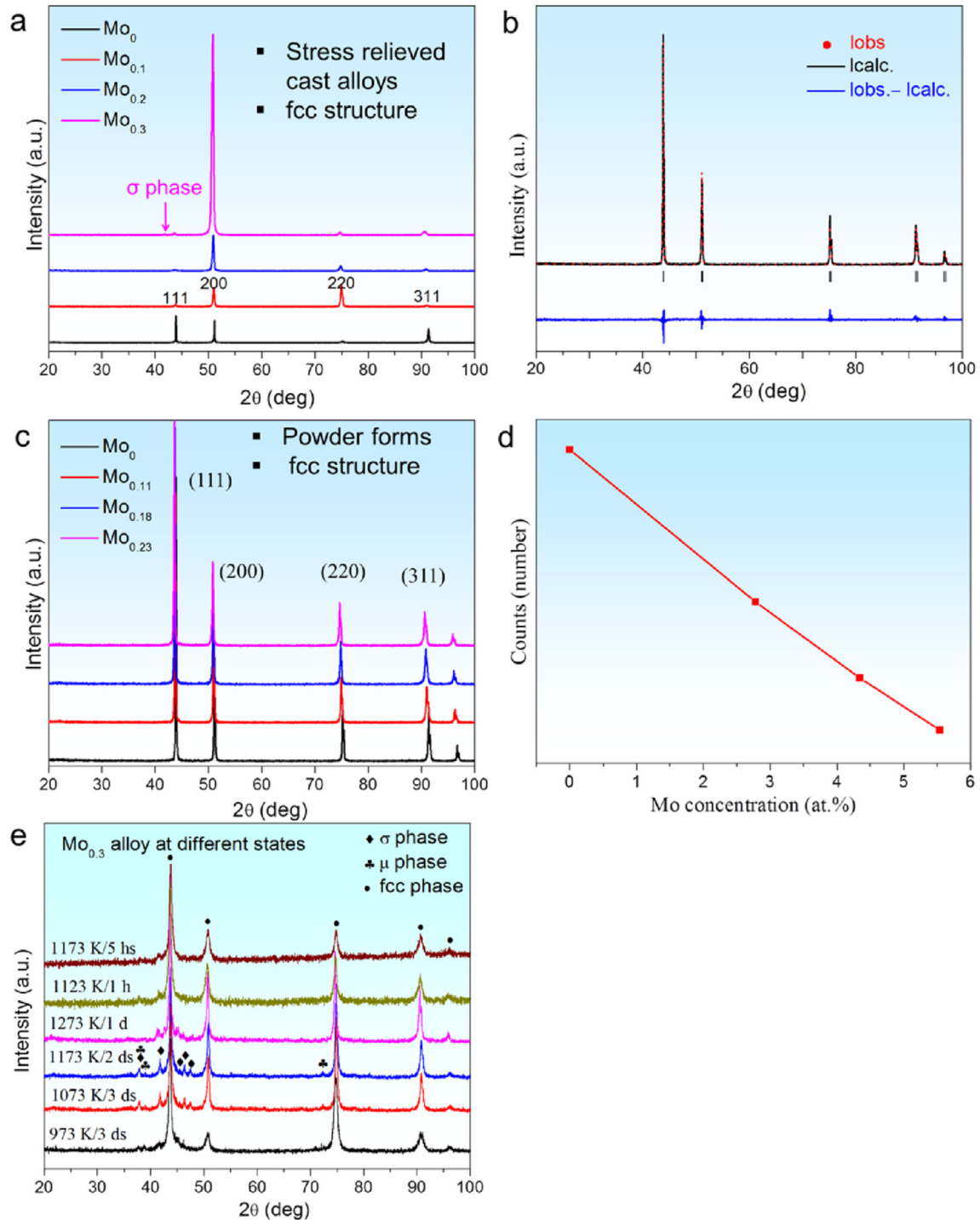


Fig. 2. XRD patterns of the (a) stress-relieved cast Mo_x ($x = 0, 0.1, 0.2$ and 0.3) alloys, (b) the Mo_x ($x = 0, 0.11, 0.18$ and 0.23) alloy powders, (c) XRD patterns (observed, calculated and difference plot) from the Rietveld refinement of the Mo_0 alloy powder, (d) (111) XRD peak intensities of the Mo_x ($x = 0, 0.11, 0.18$ and 0.23) alloy powders and (e) XRD patterns of the 60%-rolled $\text{Mo}_{0.3}$ alloy annealed at different states.

the strengthening second phases in the $\text{Mo}_{0.3}$ alloy, while to alleviate their harmful effects on ductility by controlling its morphology and dispersion. The previous study shows that the optimal age-hardening for the $\text{Mo}_{0.85}$ alloy occurs at 973 K, and the hardening effect decreases with increasing temperature [26]. However, the needle-like particles formed in the $\text{Mo}_{0.3}$ alloy at 973 K (Fig. 3e) usually cause a serious embrittlement. As a result, the 60%-rolled $\text{Mo}_{0.3}$ alloy was annealed for 1 h at 1123 K and for

5 h at 1173 K separately in order to modify the size and distribution of the hard σ and μ particles in the fcc matrix, and the microstructures are presented in Fig. 3i–l. The hard particles in the $\text{Mo}_{0.3}$ alloy annealed at 1123 K for 1 h have two main different morphologies (Fig. 3i), including retained large particles containing σ precipitates in the fcc matrix, which formed upon solidification, and relatively fine σ and μ particles precipitated from the supersaturated fcc matrix during annealing. When the annealing

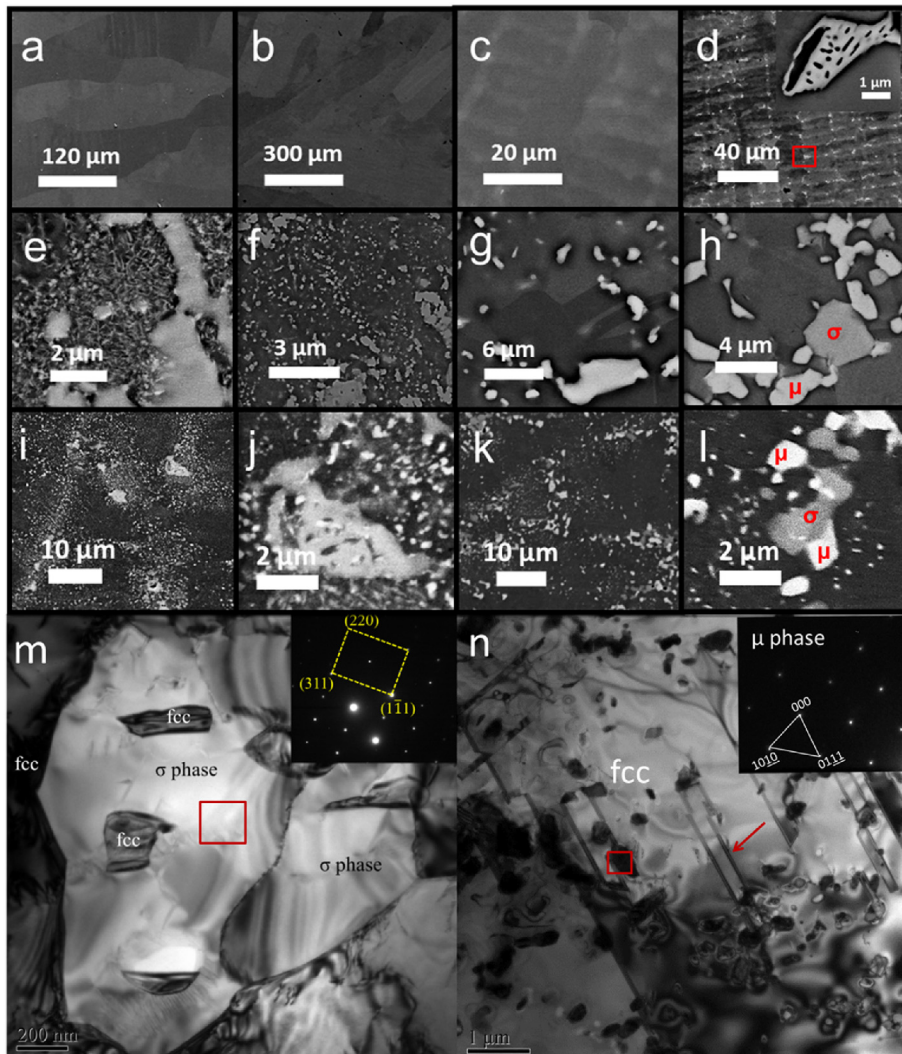


Fig. 3. SEM images of the as-cast Mo_x ((a) $x = 0$, (b) $x = 0.1$, (c) $x = 0.2$, (d) $x = 0.3$), the 60%-rolled $\text{Mo}_{0.3}$ alloy annealed at ((e) 973 K for 3 ds, (f) 1073 K for 3 ds, (g) 1173 K for 2 ds and (h) 1273 K for 1 d), the 60%-rolled $\text{Mo}_{0.3}$ alloy annealed at (i and j) 1123 K for 1 h, (k and l) 1173 K for 5 h, and TEM images and SEAD patterns of (m) the as-cast and (n) 60%-rolled and annealed at 1073 K for 3 ds $\text{Mo}_{0.3}$ alloy.

temperature increased to 1173 K, the retained large particle disappeared (Fig. 3k and l). Noted that besides the σ and μ particles precipitated from the supersaturated solid solution during annealing at temperature range of 973–1273 K, some μ phase particles appear on the fringe or inside of the σ phase formed upon casting process (Fig. 3j), which indicates that the μ phase can be transformed from the σ phase [26]. Such phase transformation process requires a necessity for cooperative diffusion of constituent atoms in order to have proper composition partitioning, all of which make the σ and μ phases show different morphologies and contrasts under the six annealed conditions (i.e., 973 K for 3 ds, 1073 K for 3 ds, 1173 K for 2 ds, 1273 K for 1 d, 1123 K for 1 h and 1173 K for 5 h). As a result, we can observe the σ and μ phases with different morphologies and contrasts under different annealing conditions (Fig. 3e–l) and even some fine μ particles precipitated out from the σ phases in Fig. 3j and l. It should be noted that although these particles are preferentially to nucleate in areas of grain boundaries or inside interdendrites, they are in discrete individual, which are crucial for a good mechanical property. Furthermore, the commonly observed annealing twinning pointed by the arrow in Fig. 3n indicates the stacking fault energy in the

$\text{Mo}_{0.3}$ alloy is extremely low, which is essential to induce deformation twinning.

3.4. Measurements of particle hardness and tensile properties of the alloys

The room-temperature nano-hardness measured by nano-indenter was carried out on the 60%-rolled $\text{Mo}_{0.3}$ alloy annealed at 1273 K for 1 d for large σ and μ particles. 32 points were carried out along a line to scan all the phases, and the result is presented in Fig. 4a. The data in the plot suggest that the σ and μ particles are much harder than that of the matrix. Noting that the hardness measured here was actually a mixture of both fine particles and the matrix and the real hardness of σ and μ particles should be much higher in the order of 15 GPa [20].

The room temperature tensile properties of the as-cast Mo_x ($x = 0, 0.2$ and 0.3) alloys were presented in Fig. 4b to thoroughly understand the solution strengthening effect of the Mo additions. The yield strength (YS), ultimate tensile strength (UTS) and elongation-to-failure (EL) are summarized in Table 3. The UTS displays a moderate improvement in the cast alloys as the Mo

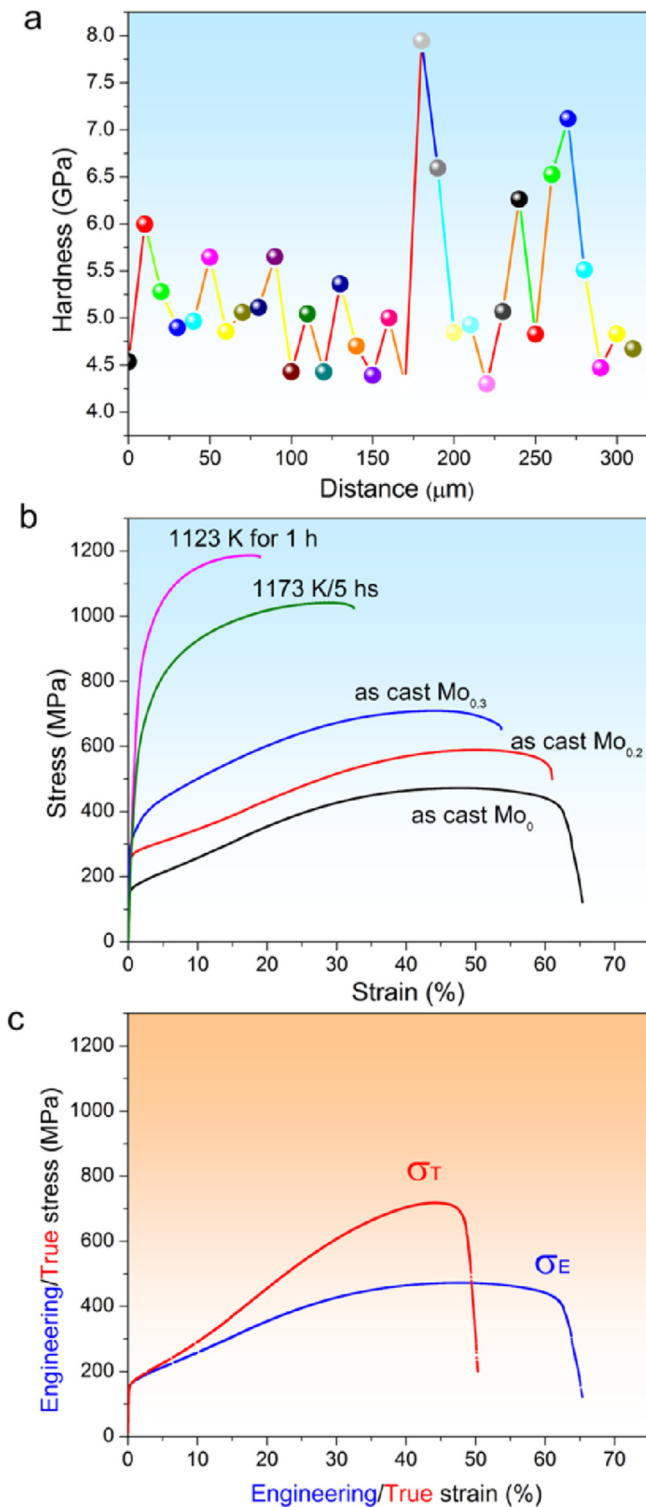


Fig. 4. (a) Nano-hardness of the σ , μ and fcc matrix of the Mo_{0.3} alloy 60%-rolled and annealed at 1273 K for 1 d. (b) room-temperature tensile engineering strain–stress curves for the as cast Mo_x ($x = 0, 0.1, 0.2$ and 0.3) alloys and the 60%-rolled Mo_{0.3} alloy annealed at different conditions, and (c) the engineering and true strain–stress curves of the as-cast Mo₀ alloy.

concentration increases from 472.4 MPa in the Mo₀ alloy to 709.7 MPa in the Mo_{0.3} alloy while the extremely good ductility was sustained with the EL slightly decreasing from 58.9% to 49.3%. The true stress (σ) and strain (ε) curve (Fig. 4c) of the as-cast Mo₀ alloy

Table 3

The yield strength (YS), ultimate tensile strength (UTS), and elongation (EL) for the as-cast Mo_x ($x = 0, 0.1, 0.2$ and 0.3) alloys and the Mo_{0.3} alloy 60%-rolled and annealed at different conditions.

Alloys	YS (MPa)	UTS (MPa)	EL (%)
As-cast Mo ₀	155.0	472.4	58.9
As-cast Mo _{0.1}	198.8	479.0	51.1
As-cast Mo _{0.2}	254.7	589.6	55.1
As-cast Mo _{0.3}	305.3	709.7	49.3
1123 K/1 h	815.5	1186.5	18.9
1173 K/5 h	646.7	1042.0	32.5
1173 K/5 h + 973 K/5 h	683.7	1066.6	30.4

shows that it has a relatively low YS 160.0 MPa but quite high UTS 718 MPa (= 4.5 \times YS), suggesting an excellent uniform deformation and very high working hardening ability.

To obtain a holistic understanding of the hardening effects of the precipitated σ and μ particles on the tensile properties of the Mo_{0.3} alloy, the engineering stress-strain curves of the Mo_{0.3} alloy 60%-rolled and annealed at 1123 K for 1 h and 1173 K for 5 h, respectively, are presented in Fig. 4b. The as-cast Mo_{0.3} alloy exhibits an extremely good ductility of EL 49.3% while a relatively low UTS 709 MPa. The strength is greatly enhanced due to the precipitation of the hard σ and μ particles. This sample exhibits a UTS about 1.2 GPa after for 1 h annealing at 1123 K while it still exhibits an attractive EL of ~19% and a phenomenally high strain hardening capability. With the annealing temperature increased to 1173 K the UTS displays a moderate decrease to ~1 GPa but the elongation increases to ~33%. A careful examination of the stress-strain curve of this sample even indicates a ductile necking effect prior to fracture.

The fracture surfaces and the longitudinal cross-section near the fracture of the deformed Mo_{0.3} alloy 60% rolled and annealed at 1173 K for 5 h were carefully examined and shown in Fig. 5. Clearly a substantial amount of small and stable cracks ($<1 \mu\text{m}$) are observed nearby the fracture surface in Fig. 5a, including particle cracking and grain boundary-precipitated particle (GB-ppt) interface cracking. Cracks mainly initiated along GB-ppt interfaces and large intermetallic particles. Measurement of the cracking orientation in the particles indicated that they cracked nearly perpendicular to the loading direction (see the inset of Fig. 5a). In other words, the particles were fractured by the principal tensile stress. Micrographs of the fracture surfaces in Fig. 5b indicate basically ductile fracture model through the nucleation and coalescence of fine microvoids.

4. Discussion

4.1. Lattice distortion and solution strengthening in HEAs

Previous characterization of the lattice distortion in HEAs was based on the diffraction intensity decrease [22] of alloys prepared by casting. However, cast alloys usually have serious preferred orientation effects, which would greatly affect the diffraction distributions of individual crystal planes. Here, powders diffraction without preferred orientation effects was utilized and the effects of large atom Mo additions on lattice distortion of the CoCrFeNi alloy were characterized carefully. Certainly, it would induce uniform strain, which causes the unit cell to expand in an isotropic way simply leading to a change in the unit cell parameters and shifting the diffraction peaks. Moreover, it may also induce non-uniform strain, which leads to systematic shifts of atoms from their ideal positions, namely local lattice distortion, and to peak broadening [27]. However, both particle size and crystal imperfections contribute to the breadth of diffraction lines on the XRD patterns

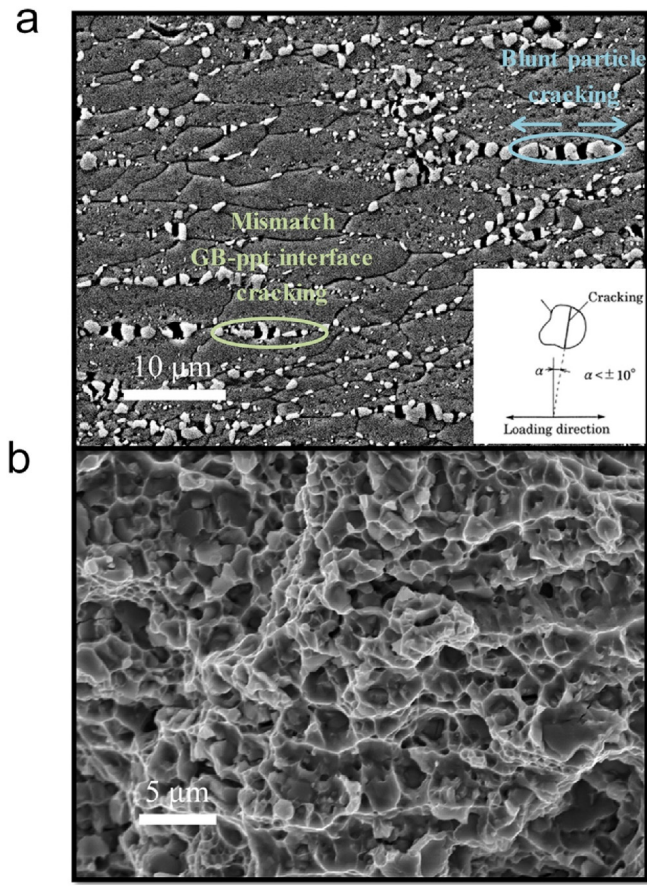


Fig. 5. (a) The longitudinal cross-section and (b) the fracture surface of the $\text{Mo}_{0.3}$ alloy 60%-rolled and annealed at 1173 K for 5 h.

[28]. In order to eliminate this effect, alloy powders with their size in the range of 5–10 μm were prepared by powder metallurgy. Thus, if there is any broadening on the diffraction crystal planes, it has to attribute to the local changes in atomic spacing caused by occupation with large Mo atoms which leads to local change in the 2θ positions for diffracted x-rays. If such broadening has a Cauchy-like profile, it can be calculated using the formula:

$$\Gamma_{hkl} = 4 \tan \theta_{estr}, \quad (1)$$

where, Γ_{hkl} is the breadth of a reflection located at 2θ and ϵ_{estr} is weighted average strain [25,29]. And the lattice distortion caused by the Mo additions in those HEA powders can be characterized by the breadth change: $(\Gamma_{hkl})_{\text{Mo}_x} - (\Gamma_{hkl})_{\text{Mo}_0}$.

The lattice parameters in both the cast and powder-metallurgy forms, which were calculated from the strongest (111) diffraction peak using MDI jade 5.0, as a function of Mo concentration are depicted in Fig. 6a. Clearly the solution of Mo results in a lattice dilation, and the lattice parameter increases continuously with the increased Mo concentration indicating a steadily growing uniform lattice strain. It should be noted that the lattice dilation of the powders is slightly larger than that of the cast alloys, and this difference should be attributed to the Mo segregation and second-phase precipitation in the cast alloys.

The widths of the Bragg diffraction lines characterized by the Full Width at Half Maximum (FWHM) of the alloy powders are presented in Fig. 6b, which represents the “width” of individual crystal planes. As indicated, the Bragg diffraction lines of the (200), (220), (311) and (111) crystal planes are all broadened with Mo

additions. As the Mo concentration increases, the broadening becomes aggravated, indicating more and more severe non-uniform lattice strain. Moreover, the results show that diffraction line broadening has strong dependence on crystal planes. The lattice distortion on crystalline planes is characterized by the change of diffraction line width [30]. Three plots are drawn with $4\tan\theta$ along the x-axis and $(\Gamma_{hkl})_{\text{Mo}_x} - (\Gamma_{hkl})_{\text{Mo}_0}$ along y-axis for all the Mo_x ($x = 0.11, 0.18$ and 0.23) powders as presented in Fig. 6c–e, all of which show a roughly linear relationship. Under this consideration, the micro-strain was assumed to be uniform in all crystallographic directions, where the material properties are independent of the direction along which they are measured. The slope of each line gives its micro-strain ϵ_{estr} existing in the powder, which increases steadily with the Mo concentration. A careful examination of the data distributions in Fig. 6c–e indicates that the experimental values of the (111) crystal planes are a little bit smaller than the fitting values. So, if the anisotropic nature of these samples was considered, the micro-strain on various planes can be calculated using Eq. (1), and the data were listed in Table 4. It can be seen that the micro-strain on the (111) planes is indeed smaller than that of other non-closely packed planes. For the large Mo atom, it has to seek a balanced lattice site in the structure unit to minimize the lattice distortion energy. The (111) plane is closely packed both on the plane and off the plane; thus larger atoms appear to be more easily to shift toward the non-closely packed planes, such as the (200) plane, this resulting in a more distortion on these non-closely packed planes. Such planar distortion is expected to provide additional hardening, and its effect will be discussed in the next part.

For HEAs, the terms “solute” and “solvent” lose their conventional meanings, thus the precise contribution of solid-solution strengthening in HEAs remains to be a challenge [1,2,5]. Fortunately, Fe, Cr, Ni, Co elements have nearly the same atomic sizes and the mixing enthalpies of different atom-pairs of these four elements are nearly equal to zero. When incorporating Mo elements at a low level to the CoCrFeNi matrix, the element will act as the solute atoms, and Fleisher's theory [31], a standard model for substitutional solid solution strengthening based on dislocation-solute elastic interactions, could be directly applied to evaluate the potency of solution strengthening caused by the solute atom of Mo. For the cast Mo_x ($x = 0, 0.1, 0.2$ and 0.3) alloys, the experimental and theoretical strength enhancement $\Delta\sigma_S$ ($\Delta\sigma_S = \sigma_{\text{Mo}_x} - \sigma_{\text{Mo}_0}$) as a function of the square root of the Mo concentration are presented in Fig. 6f. Clearly the experimental data is much higher than those of the theoretical value, suggesting an extra hardening besides the solid solution strengthening. There is an obvious reason accounting for this strength difference, that is, the alloying atoms Mo segregation and particle precipitation in the as-cast $\text{Mo}_{0.2}$ and $\text{Mo}_{0.3}$ alloys (Fig. 3c and d) which are more effective on strengthening than just solid solution hardening. What's more, the element segregation and precipitation also relaxed the lattice dilation. As illustrated in Fig. 6a, the lattice parameter of the cast alloys is smaller than that of the powders at the same composition, which would lead to the reduction of the theoretical strength enhancement. Another possible explanation may be the lattice distortion. Fleisher's theory only considered the uniform lattice dilation (change of lattice parameter); however, the stress field caused by the non-uniform lattice strain was neglected, which definitely would contribute to a certain strength improvement in the cast alloys.

4.2. Crack nucleation and ductility

In agree with our expectations, the tensile results in Fig. 4b unambiguously indicate that the hard σ and μ particles greatly harden the $\text{Mo}_{0.3}$ alloy without causing a serious embrittlement.

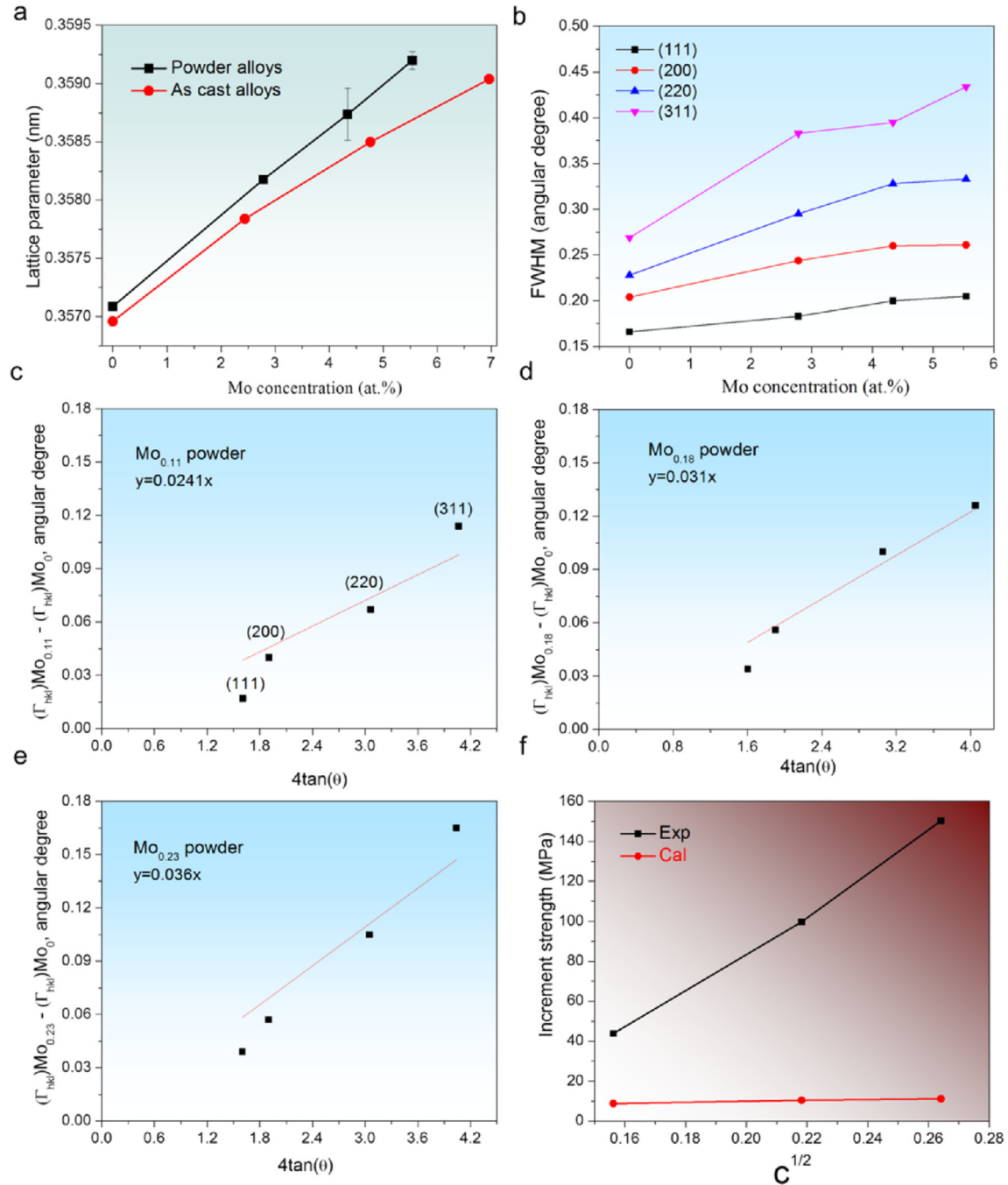


Fig. 6. (a) Lattice parameter of the as-cast Mo_x ($x = 0, 0.1, 0.2$ and 0.3) and powder-metallurgy prepared Mo_x ($x = 0, 0.11, 0.18$ and 0.23) alloys, (b) FWHM of the (111), (200), (220) and (311) crystal planes of the Mo_x ($x = 0, 0.11, 0.18$ and 0.23) alloy powders, the widths change of the Bragg diffraction lines $((\Gamma_{hk\ell})Mo_x - (\Gamma_{hk\ell})Mo_0)$ versus $4\tan\theta$ for the (c) $Mo_{0.11}$, (d) $Mo_{0.18}$ and (e) $Mo_{0.23}$ alloy powders, and (f) the theoretical and experimental solution strength caused by Mo addition, $c^{1/2}$ in the as-cast Mo_x ($x = 0.1, 0.2$ and 0.3) alloy system.

Table 4

The micro-strain of various crystal planes of the Mo_x ($x = 0.11, 0.18$ and 0.23) alloy powders.

Powders	$\varepsilon_{(111)}$ (%)	$\varepsilon_{(200)}$ (%)	$\varepsilon_{(220)}$ (%)	$\varepsilon_{(311)}$ (%)
$Mo_{0.11}$	0.011	0.021	0.022	0.028
$Mo_{0.18}$	0.021	0.029	0.033	0.031
$Mo_{0.23}$	0.024	0.030	0.034	0.041

The $Mo_{0.3}$ alloy 60% cold rolled and annealed at 1123 K for 1 h, exhibiting a tensile strength as high as 1.2 GPa and a tensile

elongation of ~19%, is selected to discuss the origin of its combination of the high strength and good ductility, from the aspect of crack nucleation and propagation.

Obviously the exceptional mechanical behavior is associated with the nature of particle distributions. Noted that these particles are essentially discrete (Fig. 3i), this just ruling out the possibility of the brittle failure due to the formation of a continuous brittle phase network. There are mainly two different morphologies particles; these large particles possessing a complex structural feature with a mixture of both the σ and fcc phases, which formed upon solidification, were essentially toughened by the ductile fcc phase; while

those discrete particles, precipitated out from the supersaturated fcc matrix during annealing process, are much fine because of the slow diffusion process in HEAs [6,32]. As shown in Fig. 5a, numerous microcracks are nucleated associated with these fine particles during plastic deformation, but their propagation has been blunted and sustained by the ductile fcc matrix.

In order to understand the ductile effect of the matrix, we need to carefully characterize the work hardening ability of the fcc matrix of the base alloy without Mo additions. To do so, we have carefully assessed the work hardening rate ($d\sigma/d\epsilon$), derived by differentiating the true stress over true strain: $d\sigma/d\epsilon$, or the strain hardening exponent (n value) of the matrix alloy from the true stress–strain ($\sigma-\epsilon$) curve obtained at room temperature. The $\sigma-\epsilon$ curve is assumed to be expressed by the Hollomon equation:

$$\sigma = Ke^n \quad (2)$$

where K is a constant, and n is referred to as the work-hardening exponent. The experimental true stress–strain ($\sigma-\epsilon$) curves were fitted with

$$\ln \sigma = \ln K + n \ln \epsilon, \quad (3)$$

which is the logarithmic form of Eq. (2). The higher n value is often related to the higher level of strengthening and toughness which effectively retard the localized deformation (suppressing crack formation and propagation) and to enhance the uniform elongation under complex stress conditions [33–35]. The work hardening exponent is generally to be a constant value; however, its value has been reported to vary with the plastic deformation in certain materials [35,36].

The work hardening rate and exponent values of our Mo_0 alloy were calculated from the yield to the ultimate tensile strength and the results are illustrated in Fig. 7a and b. These curves were obtained from raw true stress vs. strain data without employing any curve fitting techniques. As shown in Fig. 7a, the $\ln \sigma - \ln \epsilon$ curve exhibits three stages obtained by fitting with three straight lines respectively, and the slope of each line gives its respective n value. Note that the n value of the initial stage is rising slowly, followed by a rapid increase at the mid-stage, and its value finally becomes saturated at the last stage. The contribution from the mid-stage is the largest, this reflecting the key work-hardening of the HEA. Furthermore, the fcc base measured here has an unusually large work hardening exponent of 0.75. The strain hardening rate in Fig. 7b also shows three distinct stages, where stage A was characterized by a decreasing strain hardening rate, followed by stage B with an increasing strain hardening rate and then stage C with a decreasing strain hardening rate again. There are two possible explanations for such three distinguishable stages of work hardening rate in our fcc matrix. One possibility is a change in the deformation mechanism—region A: corresponding to the dislocation-slip-dominated plastic deformation, region B: the twinning-dominated plastic deformation, and region C: the dislocation-slip-dominated plastic deformation [37]. And such three different regimes of the work hardening rate points to the possible formation of a twinning-dictated deformation in our study material (Fig. 7b). First, previous studies on the fcc metals with a low stacking fault energy (SFE) strongly support the notion of deformation twinning which causes an increase in strain hardening rates [38]. The occurrence of twinning-induced plasticity behavior is generally governed by the SFE of the alloy. It was suggested [39] that deformation twinning occurs in alloys with a SFE in the range 20–50 mJ m⁻², while the Mo_0 alloy has a SFE around 30 mJ m⁻² [40]. Also, such a sudden increase of strain hardening rates during deformation at a strain rate of $1 \times 10^{-3} \text{ s}^{-1}$ at room temperature

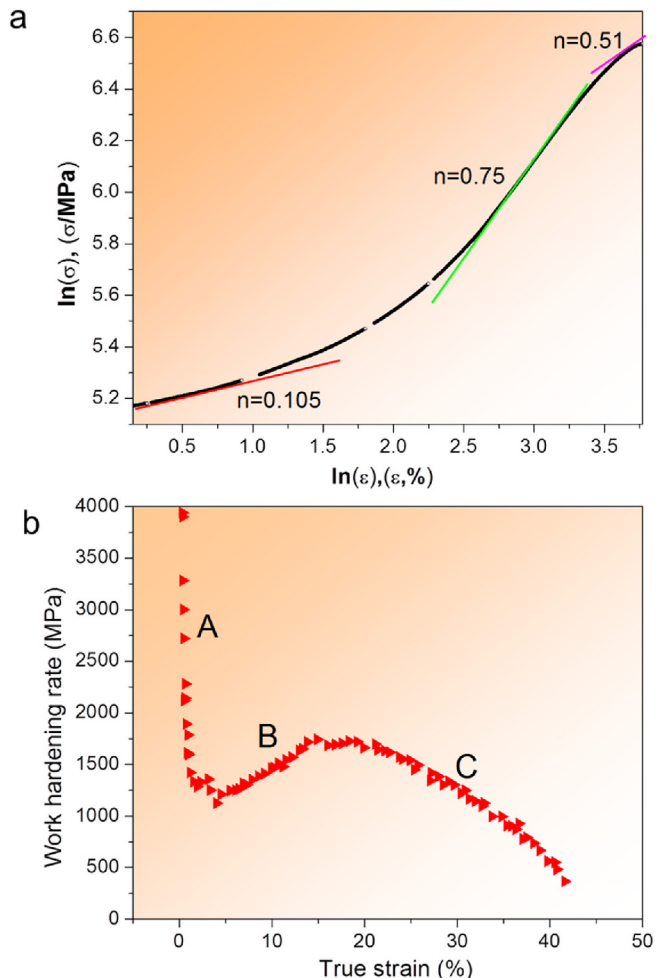


Fig. 7. The variation of strain hardening exponent (a) and rate (b) versus true strain of the as-cast Mo_0 alloy.

has been observed in high purity titanium [41], high Mn steels with twinning-induced deformation [42], and the high entropy alloy with the composition of $Al_{0.1}CrFeCoNi$ [43]. Furthermore, it is now generally recognized that when deformation was dominated by slip, the true stress–true strain curve was characterized by a higher yield point and a continuously decreased strain hardening rate from the commencement of plastic deformation. On the other hand, when deformation was governed by extension twinning, the true stress–true strain curve was reflected by a lower yield point and the strain hardening rate exhibited three distinguishable stages [37–44]. The hump in the working hardening rate of the Mo_0 alloy in Fig. 7b evidently indicate that twinning-dominated plastic deformation occurs. Another possible explanation of the increased work handing rate is related to the dissociated dislocation cores using the-state-of-the-art spherical aberration corrected TEM by Chen et al. [unpublished]. Recently they have observed widely dissociated dislocation cores in a 8% deformed $CoCrFeNiAl_{0.1}$ HEA, this leading to an extensive dislocation reaction and the formation of immobile dislocation locks (Lomer locks and Lomer-Cottrell locks) that act as the additional dislocation sources for the enhanced work hardening capacity observed in the HEA. Noted that the fcc matrix has intrinsically low SFE [40] and alloying of Mo could further reduce such energy, all of which promotes both twinning and widely dissociated and reactive dislocations. What's more, the commonly existed highly distorted lattice in HEAs could

impede the movement of the dislocations and thus may accommodate more dislocation tangle, providing additional work hardening. All the evidences discussed here suggest that it is the ductile fcc matrix with an extremely high work hardening exponent of 0.75 that suppresses the immediate propagation of microcracks associated with hard particles in the Mo_{0.3} alloy and thus contributes a combination of high strength and good ductility of this HEA.

5. Conclusion

The alloy design principle generally suggests the suppression of ‘brittle’ intermetallic compound formation which seriously embrittles structure materials during plastic deformation. To against this common alloy design principle, we are on purposely added those brittle but hard particles in the ductile fcc CoCrFeNi HEAs to strengthen them through a computational-aided alloy design approach. It was found that the alloying of Mo into the CoCrFeNi HEA catalyzes precipitation of brittle but extremely hard σ and μ intermetallics in the fcc matrix; surprisingly, we reveal that such precipitation tremendously strengthen the Mo_{0.3} alloy but without causing serious embrittlement. The particle-strengthened alloy exhibits a tensile strength as high as 1.2 GPa and a tensile elongation of ~19% at ambient temperature. Major efforts have thus been devoted to characterize the structures and properties of these intermetallic particles in this alloy. Both large complex σ phase and fine σ and μ intermetallic phases are formed in the Mo_{0.3} alloy as detected by TEM analyses. Nanoindentor measurements reveal that these particles have a hardness at least higher than 8 GPa. However, some intermetallic particles, even large but possessing a complex structural feature on solidification, are toughened by the ductile fcc matrix phase. While those particles precipitated out from the supersaturated fcc matrix are relatively fine because of the slow diffusion process in HEAs, and they are very effective in strengthening the alloy. The study of mechanical behavior of the (CoCrFeNi) matrix reveals an extremely high work-hardening exponent of 0.75, which promotes a uniform deformation and suppresses microcrack propagation associated with these particles. All of these contribute to a high fracture strength and decent ductility of the Mo_{0.3} alloy hardened by σ and μ particles. Our study presents a very successful demonstration of using complex hard and brittle intermetallic particles to manipulate the properties of fcc-type (CoCrNiFe) HEA system with Mo additions, and the gained findings are important not only for the understanding of the strengthening mechanism of these emerging metallic materials, but also for the future development of high-performance HEAs for engineering applications. Furthermore, XRD analysis of the Mo_x powders produced by powder metallurgy exhibits a simple fcc structure without preferred orientation effects. The measurement of diffraction line broadening confirmed that the lattice is highly distorted in HEAs.

Acknowledgements

This research was supported by the Hong Kong Government through the General Research Fund (GRF) with the grant number of CityU 11209314. B. Liu and Y. Liu were supported by the State Key Laboratory of Power Metallurgy, Central South University (CSU) (2015cx004), and the grant from the project of Innovation-driven Plan in CSU of China.

References

- [1] J.W. Yeh, S.K. Chen, S.J. Lin, J.Y. Gan, T.S. Chin, T.T. Shun, C.H. Tsau, S.Y. Chang, Nanostructured high-entropy alloys with multiple principal elements: novel alloy design concepts and outcomes, *Adv. Eng. Mater.* 6 (2004) 299–303.
- [2] B. Cantor, I.T.H. Chang, P. Knight, A.J.B. Vincent, Microstructural development in equiatomic multicomponent alloys, *Mater. Sci. Eng. A* 375 (2004) 213–218.
- [3] Senkov, J.D. Miller, D.B. Miracle, C. Woodward, Accelerated exploration of multi-principal element alloys with solid solution phases, *Nat. Commun.* 6 (2015) 4.
- [4] M.S. Lucas, G.B. Wilks, L. Mauger, J.A. Munoz, O.N. Senkov, Absence of long-range chemical ordering in equimolar FeCoCrNi, *Appl. Phys. Lett.* 100 (2012) 251907.
- [5] Z. Wang, Y. Huang, Y. Yang, J. Wang, C.T. Liu, Atomic-size effect and solid solubility of multicomponent alloys, *Scr. Mater.* 94 (2015) 28–31.
- [6] W.H. Liu, Y. Wu, J.Y. He, T.G. Nieh, Z.P. Lu, Grain growth and the Hall-Petch relationship in a high-entropy FeCrNiCoMn alloy, *Scr. Mater.* 68 (2013) 526–529.
- [7] A. Takeuchi, K. Amiya, T. Wada, K. Yubuta, W. Zhang, High-entropy alloys with a hexagonal close-packed structure designed by equi-atomic alloy strategy and binary phase diagrams, *JOM* 66 (2014) 1984–1992.
- [8] Senkov, S.V. Senkova, C.F. Woodward, Effect of aluminum on the microstructure and properties of two refractory high-entropy alloys, *Acta Mater.* 68 (2014) 214–228.
- [9] K.M. Youssef, A.J. Zaddach, C. Niu, D.L. Irving, C.C. Koch, A novel low-density, high-hardness, high-entropy alloy with close-packed single-phase nanocrystalline structures, *Mater. Res. Lett.* 3 (2014) 95–99.
- [10] Y. Zhang, T.T. Zuo, Z. Tang, M.C. Gao, K.A. Dahmen, P.K. Liaw, Z.P. Lu, Microstructures and properties of high-entropy alloys, *Prog. Mater. Sci.* 61 (2014) 1–93.
- [11] B. Gludovatz, A. Hohenwarter, D. Catoor, E.H. Chang, E.P. George, R.O. Ritchie, A fracture-resistant high-entropy alloy for cryogenic applications, *Science* 345 (2014) 1153–1158.
- [12] Y. Zou, H. Ma, R. Spolenak, Ultrastrong ductile and stable high-entropy alloys at small scales, *Nat. Commun.* 6 (2015).
- [13] W.H. Liu, J.Y. He, H.L. Huang, H. Wang, Z.P. Lu, C.T. Liu, Effects of Nb additions on the microstructure and mechanical property of CoCrFeNi high-entropy alloys, *Intermetallics* 60 (2015) 1–8.
- [14] Y. Wu, W.H. Liu, X.L. Wang, D. Ma, A.D. Stoica, T.G. Nieh, Z.B. He, Z.P. Lu, In-situ neutron diffraction study of deformation behavior of a multi-component high-entropy alloy, *Appl. Phys. Lett.* 104 (2014) 051910.
- [15] F. Otto, A. Dlouhy, C. Somsen, H. Bei, G. Eggeler, E.P. George, The influences of temperature and microstructure on the tensile properties of a CoCrFeMnNi high-entropy alloy, *Acta Mater.* 61 (2013) 5743–5755.
- [16] B. Schuh, F. Mendez-Martin, B. Völker, E.P. George, H. Clemens, R. Pippan, A. Hohenwarter, Mechanical properties, microstructure and thermal stability of a nanocrystalline CoCrFeMnNi high-entropy alloy after severe plastic deformation, *Acta Mater.* 96 (2015) 258–268.
- [17] Z. Fu, W. Chen, H. Wen, D. Zhang, Z. Chen, B. Zheng, Y. Zhou, E.J. Lavernia, Microstructure and strengthening mechanisms in an FCC structured single-phase nanocrystalline Co₂₅Ni₂₅Fe₂₅Al_{7.5}Cu_{17.5} high-entropy alloy, *Acta Mater.* 107 (2016) 59–71.
- [18] Z.K. Teng, G. Ghosh, M.K. Miller, S. Huang, B. Clausen, D.W. Brown, P.K. Liaw, Neutron-diffraction study and modeling of the lattice parameters of a NiAl-precipitate-strengthened Fe-based alloy, *Acta Mater.* 60 (2012) 5362–5369.
- [19] Z. Sun, C.H. Liebscher, S. Huang, Z. Teng, G. Song, G. Wang, M. Asta, M. Rawlings, M.E. Fine, P.K. Liaw, New design aspects of creep-resistant NiAl-strengthened ferritic alloys, *Scr. Mater.* 68 (2013) 384–388.
- [20] H. ur Rehman, K. Durst, S. Neumeier, A.B. Parsa, A. Kostka, G. Eggeler, M. Göken, Nanoindentation studies of the mechanical properties of the μ phase in a creep deformed Re containing nickel-based superalloy, *Mater. Sci. Eng. A* 634 (2015) 202–208.
- [21] C.M.F. Rae, R.C. Reed, The precipitation of topologically close-packed phases in rhodium containing superalloys, *Acta Mater.* 49 (2001) 4113–4125.
- [22] J.Y. He, H. Wang, H.L. Huang, X.D. Xu, M.W. Chen, Y. Wu, X.J. Liu, T.G. Nieh, K. An, Z.P. Lu, A precipitation-harden high-entropy alloy with outstanding tensile properties, *Acta Mater.* 102 (2016) 187–196.
- [23] J.O. Andersson, T. Helander, L. Höglund, P. Shi, B. Sundman, Thermo-calc & DICTRA, computational tools for materials science, *Calphad* 26 (2002) 273–312.
- [24] J.W. Yeh, S.Y. Chang, Y.D. Hong, S.K. Chen, S.J. Lin, Anomalous decrease in X-ray diffraction intensities of Cu–Ni–Al–Co–Cr–Fe–Si alloy systems with multi-principal elements, *Mater. Chem. Phys.* 103 (2007) 41–46.
- [25] L.B. McCusker, R.B. Von Dreele, D.E. Cox, D. Louer, P. Scardi, Rietveld refinement guidelines, *J. Appl. Cryst.* 32 (1999) 36–50.
- [26] T.T. Shun, L.Y. Chang, M.H. Shiu, Age-hardening of the CoCrFeNiMo0.85 high-entropy alloy, *Mater. Charact.* 81 (2013) 92–96.
- [27] A.R. Stokes, A.J.C. Wilson, The diffraction of X rays by distorted crystal aggregates-I, *Proc. Phys. Soc.* 56 (1944) 174.
- [28] R. Delhez, T.H. De Keijser, J.I. Langford, D. Louer, E.J. Mittemeijer, E.J. Sonneveld, Crystal imperfection broadening and peak shape in the Rietveld method, *Rietveld Method* 5 (1993) 132–166.
- [29] G.K. Williamson, W.H. Hall, X-ray line broadening from filed aluminium and wolfram, *Acta Metall.* 1 (1953) 22–31.
- [30] R. Delhez, T.H. De Keijser, E.J. Mittemeijer, Determination of crystallite size and lattice distortions through X-ray diffraction line profile analysis, *Fresenius Z. Anal. Chem.* 312 (1982) 1–16.
- [31] R.L. Fleischer, Substitutional solution hardening, *Acta Metall.* 11 (1963) 203–209.
- [32] K.Y. Tsai, M.H. Tsai, J.W. Yeh, Sluggish diffusion in Co–Cr–Fe–Mn–Ni high-entropy alloys, *Acta Mater.* 61 (2013) 4887–4897.
- [33] P. Antoine, S. Vandepitte, J.B. Vogt, Empirical model predicting the value of

- the strain-hardening exponent of a Ti-IF steel grade, *Mater. Sci. Eng. A* 433 (2006) 55–63.
- [34] M. Umemoto, K. Tsuchiya, Z.G. Liu, S. Sugimoto, Tensile stress-strain analysis of single-structure steels, *Mater. Trans. A* 31 (2000) 1785–1794.
 - [35] T. Xu, Y. Feng, Z. Jin, S. Song, D. Wang, Determination of the maximum strain-hardening exponent, *Mater. Sci. Eng. A* 550 (2012) 80–86.
 - [36] A.K. Sachdev, Effect of retained austenite on the yielding and deformation behavior of a dual phase steel, *Acta Metall.* 31 (1983) 2037–2042.
 - [37] A. Rohatgi, K.S. Vecchio, G.T. Gray III, The influence of stacking fault energy on the mechanical behavior of Cu and Cu-Al alloys: deformation twinning, work hardening, and dynamic recovery, *Mater. Trans. A* 32 (2001) 135–145.
 - [38] S. Asgari, E. El-Danaf, S.R. Kalidindi, R.D. Doherty, Strain hardening regimes and microstructural evolution during large strain compression of low stacking fault energy fcc alloys that form deformation twins, *Mater. Trans. A* 28 (1997) 1781.
 - [39] L. Remy, A. Pineau, Twinning and strain-induced fcc → hcp transformation in the Fe-Mn-Cr-C system, *Mater. Sci. Eng.* 26 (1976) 123.
 - [40] A.J. Zaddach, C. Niu, C.C. Koch, D.L. Irving, Mechanical properties and stacking fault energies of NiFeCrCoMn high-entropy alloy, *JOM* 65 (2013) 1780–1789.
 - [41] A.A. Salem, S.R. Kalidindi, R.D. Doherty, Strain hardening regimes and microstructure evolution during large strain compression of high purity titanium, *Scr. Mater.* 46 (2002) 419–423.
 - [42] H. Beladi, I.B. Timokhina, Y. Estrin, J. Kim, B.C. De Cooman, S.K. Kim, Orientation dependence of twinning and strain hardening behavior of a high manganese twinning induced plasticity steel with polycrystalline structure, *Acta Mater.* 59 (2011) 7787–7799.
 - [43] N. Kumar, Q. Ying, X. Nie, R.S. Mishra, Z. Tang, P.K. Liaw, R.E. Brennan, K.J. Doherty, K.C. Cho, High strain-rate compressive deformation behavior of the Al0.1CrFeCoNi high entropy alloy, *Mater. Des.* 86 (2015) 598–602.
 - [44] H. Beladi, I.B. Timokhina, Y. Estrin, J. Kim, B.C. De Cooman, S.K. Kim, Orientation dependence of twinning and strain hardening behavior of a high manganese twinning induced plasticity steel with polycrystalline structure, *Acta Mater.* 59 (2011) 7787–7799.